The Extended Hydrogen Bond: A Coupling Pair of Flexible and Polarizable Dipoles

(8 displays, 250 words abstract, 10000 words, 95 refs)

Chang Q Sun[1*]

Abstract

Being essential to life on earth, the hydrogen bond and its configuration, performance, and functionality become increasingly inspiring. We humbly share a three-body coupling X:R-Y system involving a pair of retractable and polarizable Z-X and R-Y dipoles. The (:) is the negative polar end of a dipole. The R is not limited to hydrogen. The X:R-Y bond covers at least four situations, meets the unique criterion of force combination, and possesses at least five characteristics. Specifically, the lone-pair-engaged N/O:H-O/N/C bonds feature properly the performances of H_2O and CHNO molecular assemblies; the dipolar M^P or atomic vacancy V^0 replaced M^P/V^0:R-Y bonds could coordinate molecular physisorption for catalysis and hydrogen storage; and the polarity-inverted M^+-O^{2-}:M^P formed during chemisorption drives the oxidation bonding and electronic dynamics. The combination of X:R attraction and X:⇔:Y repulsion is decisive to the performance of the X:R-Y system that follows the hydrogen bond cooperability and polarizability (HBCP) regulation in the segmental length, energy, and specific heat [Sun et al, *Phys Rep* 2023; 998:1-68]. The X:R-Y exhibits extraordinary adaptivity, recoverability, sensitivity, catalytic capability, and chemical reactivity. A perturbation such as mechanical compression, thermal loading, electronic polarization, or molecular undercoordination changes the X—Y distance by lengthening one segment and shortening the other. The HBCP premise has substantiated the understanding of water ice anomalies, molecular hydration interfaces, CHNO energetic assemblies, and oxygen chemisorption, inspiring promising ways of thinking about single-atom catalysis and low-dimensional high-T_C superconductivity. Further extension of the amplification to other areas such as biological science and cell engineering would be even more fascinating and promising.

[1] RISE & School of Materials Science & Engineering, Dongguan University of Technology, Dongguan 523808, China (2022130@dgut.edu.cn; ecqsun@ntu.edu.sg)

TOC Entry

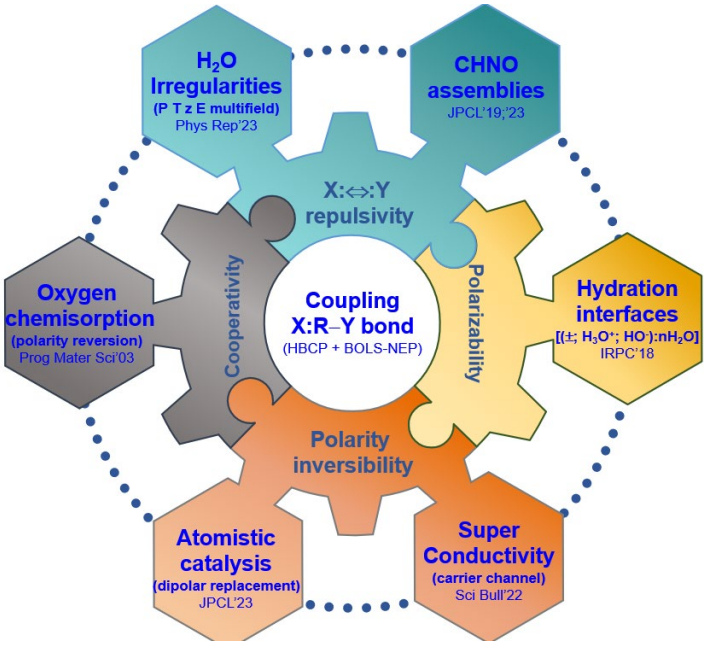

Or

Three types of X:R-Y bonds meet unique force criterion and possess extraordinary adaptivity, disparity, polarizability, recoverability, sensitivity, reactivity and catalytic capability ($F_{A/R}$ for attractive/repulsive force):

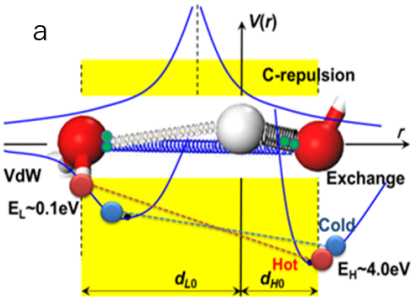

Lone-pair-involved
N/O:H-O/N/C
for H_2O & CHNO
assemblies

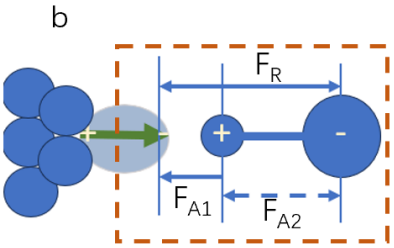

Dipolar-replaced
M^P:R^+-Y^-
for physisorption
& atomic catalysis

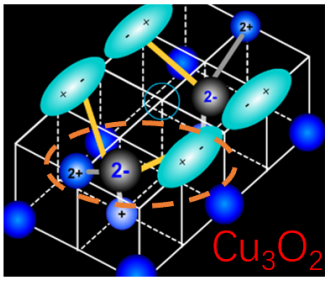

Polarity-inverted
Cu^+-O^{2-}:Cu^P
for chemisorption &
superconductivity

Contents

1 Introduction

The hydrogen bond is ubiquitous and important yet its configuration, performance, and functionality remain an issue of challenging [1-4]. The IUPAC-recommended Z−X···H−Y bonding system focuses mainly on the X···R attraction and refers the X···R to the hydrogen bond by assuming both the Z−X and the H−Y as less dependent, non-polarizable, and rigid[5]. The H is less electronegative than X and Y. The X···H attraction is named nonbond because there is little charge sharing between X and H.

Having about 0.1-0.2 eV cohesive energy, the weak X···H nonbond interaction could involve multiple factors[6] such as electrostatic interactions, charge transfer, p-resonance assistance, steric repulsion, cooperative effects, dispersion, and secondary-electrostatic interaction, in addition to delocalization of the paired or unpaired lone electrons[7, 8] and nuclear quantum effect for lighter atoms specifically[9, 10]. The two-body X···H system has been succeeded in describing intermolecular interactions[5] and molecular dynamics in processes such as ice nucleation[11], liquid-solid transition[12], evaporation[13], molecular motion under a certain kind of perturbation, and the lifespan of a molecule residing in a specific location[14]. An extension[15, 16] suggests that the hydrogen bond should include the polarity-inversion involving non-classical hydridic and dihydrogen formation, meeting the requirement of X···H attraction.

From the two-body O···H nonbond perspective, one often takes an H_2O molecule as the primary structural unit, such as the TIPnQ model series ($n \leq 5$)[17, 18] in dealing with the manner and mobility of motion for a water molecule that is approximated as a rigid dipole consisting of n fixed point charges and constant H-O length and ∠H-O-H angle. However, it remains challenging to accurately predict water's phase diagram and anomalies due to the missing link between the strong intramolecular H-O bond and the weak intermolecular O···H interactions[18, 19].

From the perspective of Hamiltonian perturbation[20], one may realize that bonds and electrons are carriers of energy and the primary building blocks. Relaxation of bond length and energy and polarization of electrons dictate the performance of a substance of concern and determine the manner and mobility of proton or molecule motion. It would be necessary to consider the cooperativity, disparity, flexibility, and polarizability of the three-body coupling O:H-O bond that couples the polarizable and flexible H-O dipoles as a unit with ":" being the electron lone of oxygen formed upon

reaction taking place [21]. For structure periodicity consideration, the O:H-O is inclusive for inter- and intramolecular cooperative interactions.

Intensive spectroscopic evidence has shown that when subjected to a perturbation such as mechanical compression[22], thermal loading[23, 24], electrification[25], solvation charge injection[26, 27], and molecular undercoordination[28], or their combinations, the vibration frequency (ω_L) of the O:H nonbond shifts in the range of 75-250 cm^{-1} while the ω_H of the H-O polar-covalent bond shifts cooperatively, disparately, and oppositely in the range of 3600-3200 cm^{-1}. If a perturbation stiffens the ω_H, the ω_L will become softer, and vice versa. It is the O:H-O segmental phonon cooperative relaxation under heating[23] and compression[29] that has inspired the initiation of introducing the O:⇔:O repulsive coupling interaction[30]. The polarizability and cooperativity of the O:H-O segmental length and energy and the ∠O:H-O angle dictate water's properties, and therefore, the three-body coupling O:H-O bond should be the primary unit for structure change and energetic exchange of water.

In this Perspective, we humbly share our findings and understandings accumulated in the past three decades in developing the three-body coupling X:R-Y bond, from the standing point of Hamiltonian perturbation-driven bonding and electronic dynamics. As an amplification of the O:H-O, the X:R-Y must meet a certain number of criterion, be more generalization, follow certain regulations, and possess common characteristics, as detailed in subsequent sections. Therefore, the R is not limited to hydrogen.

The presentation is arranged as follows. Section 1 overviews the status and challenging issues of hydrogen bond relevance. Section 2 introduces the basic regulations of hydrogen bond cooperativity and polarizability (HBCP)[31] for the coupling system and the bond order-length-strength correlation and nonbonding electron polarization (BOSL-NEP)[32] for the effect of atomic/molecular undercoordination. Section 3 discusses the essentiality, criteria, and characteristics of the X:R-Y coupling systems including electron lone pair engagement, dipolar replacement, and charge polarity inversion.

Section 4 briefly introduces the O:H-O bond and its performance and functionality on water properties. Section 5 describes the O:H-O extension to the O/N:H-N/C for the structural stability and energy storage of the CHNO molecular assemblies[33-36]. Water and explosives share the same kind of hydrogen bonds whose covalent part expands under compression and contracts when heated. Section 6 shares our findings on the bond relaxation in the hydration cells of acid, base, and salt solutions [26].

Section 7 justifies the dipolar M^P- or atomic vacancy V^0 substituted M^P/V^0:R-Y bond that follows the HBCP and the BOS-NEP regulation, showing the undercoordination derived bond contraction, core band entrapment, and the valence electron polarization. Ether the undercoordinated M^P or the V^0 replaces the X: dipole providing the negative polar end of electron rich. An uncoordinated Rh^P dipole forms the Rh^P:H-C bond with an adsorbed CH_4 molecule. The combination of the Rh^P:H attraction and the Rh^P:⇔C repulsion stretches and weakens the H-C toward dissociation. Section 8 addresses the polarity-inverted M^P:R-Y bond (Cu^+-O^{2-}:Cu^P) presented during oxygen chemisorption on the Cu(100;110) surfaces. The Cu^+-O^{2-}:Cu^P relaxation and polarization, the O-Cu chains and the Cu_2O planes should be potential elements contributing to the low-dimensional high-T_C superconductivity.

The last section 9 summarizes the present contribution and provides a perspective on future directions. The response of the coupling pair of the elastic and polarizable dipoles would suffice to deal with the strongly correlated systems. Further extension of the presented exercises should be even more fascinating and rewarding.

2 The HBCP and BOLS-NEP regulations

The notion of HBCP[31] for the effect of the X:⇔:Y repulsive coupling regulates the performance of the X:R-Y bond when subjected to a perturbation. The BOLS-NEP[32] correlation dictates the performance of any bond between undercoordinated atoms or the intramolecular bond of an undercoordinated molecule. **Fig. 1** plots and illustrates these regulations:

Regulation	BOLS-NEP[32, 37]	HBCP for O:H-O[30, 31]
Formulation	$\begin{cases} C_z & = d_z/d_b = 2/\{1+exp[(12-z)/(8z)]\} \\ C_z^{-m} & = E_z/E_b \end{cases}$	$\begin{cases} d_{OO} & = 2.6950\rho^{-1/3} \\ d_L/d_{L0} & = 2/\{1+exp[(d_H-d_{H0})/0.2428]\} \end{cases}$
Notation	Bond contraction coefficient C_z, Coordination number z (or CN), bond length d, bond energy E, bond nature index m, subscript of bulk b.	Mass density ρ, O—O distance d_{OO}, O:H length d_L, H-O length d_H, ρ = 1, d_{L0} = 1.6946, and d_{H0} = 1.0004 Å are bulk reference at 277 K for H_2O:$4H_2O$ tetrahedron configurated structure.

Indication	Atomic or molecular undercoordination shortens and strengthens the bonds between undercoordinated atoms, associated with the core and bonding electron self-entrapment and nonbonding electron polarization.	The X:⇔:Y repulsion drives the X:R-Y to relax cooperatively its segmental length, energy, and specific heat associated with polarization or thermal depolarization when subjected to perturbation.
Evidence	· 30% bond contraction for monatomic chains and graphene edges[32]. · 12% for the fcc(001) first layer spacing [21]. · 10% H−O bond contraction of water droplets[38]. · Bond contraction happens to the outermost two atomic layer spacings[38, 39].	· Liquid heating stiffens the H-O and softens the O:H phonons associated with depolarization[23, 24] · Compression stiffens the O:H and softens the H-O toward O:H-O segmental length symmetry associated with depolarization[29]. · Molecular undercoordination[28] or electrification[26] stiffens the H-O and softens the O:H.

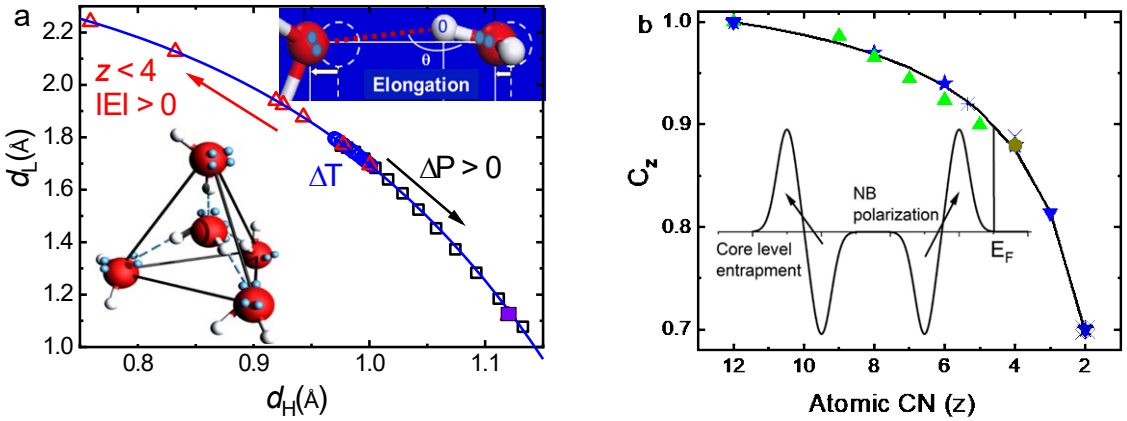

Fig. 1 | HBCP[31] and BOLS-NEP[32] regulations. (a) The O:H (d_L) and H−O (d_H) length cooperative relaxation under perturbation of pressure (P), temperature (T), electric field (E), and molecular coordination (z) with inset showing the H_2O:4H_2O tetrahedron with conservation of the number and orientation of the O:H-O bonds. The upper right inset illustrates the O:H-O segmental length cooperative relaxation with respect to the coordination origin H. The θ is the ∠O:H-O bond angle. A perturbation changes the O—O distance by shortening one segment and lengthening the other due to O—O repulsive coupling. (b) The atomic-CN resolved bond length contraction, core band quantum entrapment, and nonbonding electron polarization (inset).

3 Criteria and characteristics of the X:R-Y bond

The amplified X:R-Y bond integrates two flexible and polarizable dipoles, Z-X and R-Y. The Z can be free from the X:R-Y for the structure periodicity reason, as the X:R-Y could be sufficient to feature the inter- and intramolecular interactions for the entire bonding network. The coupling X:R-Y bond length and energy are inclusive of necessary parameters determining the performance and functionality of the bonding system.

The X:R-Y bond must meet the unique criterion of force combination:

1) **Force combination.** The X:R Columb attraction and the X:⇔:Y repulsion pair up the Z-X and R-Y dipoles. The X:⇔:Y repulsion not only equilibrates the inter-dipolar X:R attraction but also correlates the inter-dipolar X:R nonbond and the intra-dipolar R-Y polar-covalent bond, which dictates the performance and functionality of the X:R-Y bonding system when responding to a perturbation. The R-Y can be covalently bonded such as H_2 that turns to be an instantaneous $H^{\delta+}$-$H^{\delta-}$ dipole under the force of London dispersion. The X:R-Y follows the HBCP regulation, provided that the X:⇔:Y repulsion is sufficiently strong. Therefore, any three-body interaction meets this criterion can be categorized into the extended hydrogen bond, without needing electronegativity discrimination.

Following the HBCP and BOLS-NEP regulations, the X:R-Y bond may have the following characteristics:

1) **Length and energetic disparity.** The X:R and R-Y have discriminative length, energy, and vibration frequency. For the O:H-O instance, the cohesive energy of O:H is 0.1-0.2 eV, and vibrates at 75-200 cm^{-1} frequencies as compared to the H-O bond that has 5.1-4.0 eV cohesive energy and vibrates at a faster pace of 3700-3200 cm^{-1}.[31] One can only break the H-O bond in gaseous phases by a 121.6 nm laser beam radiation. [40] The vibration frequency depends on the length (d) and energy (E) in the form of $\omega^2 \propto E/d^2 \propto Yd$, with Yd being the stiffness of the oscillator and the elastic modulus $Y \propto E/d^3$.

2) **Specific heat disparity.** The vibration frequency ω and the cohesive energy E of a segment uniquely determine its specific heat $\eta(\theta, \Theta_D)$. The ω defines the Debye temperature (Θ_D) according to Einstein's relation of ω/Θ_D = constant. The integral of the specific heat $\eta(\theta, \Theta_D)$ up to the temperature of thermal dissociation equals the segmental cohesive energy E. As a result, the (200

cm^{-1}, 0.2 eV)$_L$ for the O:H nonbond and the (3200 cm^{-1}, 4.0 eV)$_H$ for the H-O bond discriminate the segmental specific heats[24].

3) **Strong cooperativity and polarizability.** When a perturbation occurs, the X:R-Y responds cooperatively, disparately in length scale, and oppositely in direction. For instance, when under compression, the H-O/N bonds expand, the O:H nonbond contracts, toward O:H-O segmental lengths symmetrisation [41]. Conversely, when the O:H-O/N undergoes molecular undercoordination, vacuuming, electrostatic polarization, or liquid and ice-I heating, it relaxes in a contrasting way due to the strong X:⇔:Y repulsion, see FIG. 3a-e in the Section 4. The X:⇔:Y Columb repulsion polarizes the nonbonding electrons of X and Y, and the extent of polarization depends on their charge quantities and separation.

4) **Extraordinary adaptivity, recoverability, and sensitivity**. The combination of the X:R attraction and the X:⇔:Y repulsion makes the soft X:R oscillator extremely elastic and sensitive to a perturbation[42, 43], which ensures the extraordinary adaptivity and recoverability of the entire X:R-Y bonding system to a perturbation, such as ice slipperiness[44] and skin hydrophobicity of water and superfluidity of droplets traveling in microchannels [45].

5) **High catalytic capability and chemical reactivity**. When subjected to molecular undercoordination, the X:R-Y systems show high chemical reactivity and catalytic capability[46, 47] because of the local strong electric field of the enhanced dipoles that gather electrons from the H^+ to O^{2-} of the surface H_2O molecules.[48, 49] The surface dipoles make the "on-water catalyst" that accelerates substantially reaction rate [50, 51] and the hydro-voltaicity for electricity harvesting.

FIG. 2 illustrates typical configurations of the X:R-Y bond [21, 31, 34] – electron lone pair (:) engagement, dipolar or atomic vacancy replacement, and negativity polarity inversion. The X:R-Y bond meets the unique criterion of force combination, follows the HBCP regulation under perturbation, and the BOLS-NEP when subjected to molecular undercoordination.

In the first situation involving electron lone pair or equivalent such as unpaired π-bonding electrons, see FIG. 2a, R denotes any atom of less electronegative than Y and X. X refers to the negative part of the Z-X dipole with ":" being the negative polar end of electron-rich, pointing towards the positive R that acts as the coordination origin of the X:R-Y system. The X:R nonbond is identical to the

convention of X···R attraction [5] but it would be clearer to discriminate the lone pair contribution. Typical examples include X = O (3.5), N (3.0); Y = X, C (2.5); and R = H (2.2), with brackets specifying their electronegativity values.

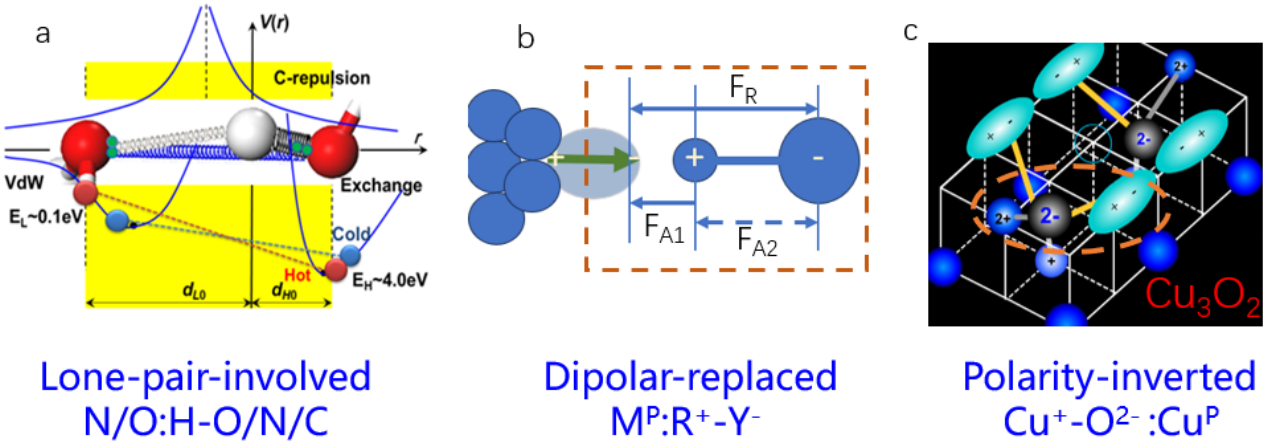

FIG. 2| **Possible X:R-Y bond configurations as framed.** (a) Lone-pair-engaged N/O:H-O/N/C bonds for H_2O and CHNO molecular assemblies[33, 34]. The O—O repulsion couple the intermolecular O:H nonbond (vdW, should be an attraction between the lone-pair and the proton, instead) and the intramolecular H-O polar-covalent bond (exchange interaction), driving the HB follows the HBCP regulation when perturbed. (b) Dipolar (vacancy)-substituted M^P:R^+-Y^- bond for molecular physisorption and single-atom catalysis. F_R and F_A denote the repulsion and attraction, respectively. The protruding M^P polarizes and stretches the R-Y dipole by repelling Y^- and attracting R^+. Atomic vacancy shares the same function of polarization. (c) Polarity-inverted M^+-O^{2-}:M^p bond for oxygen chemisorption on Cu(100) surface. Formation of the Cu_3O_2 pairing etrahedron[21] results in layer spacing expansion, oppositely coupled Cu^P:⇔:Cu^P crossing the missing row vacancies, which derived the O-Cu chains and Cu_2O planes for the low-dimensional high-T_C superconductivity[52].

On the second occasion, FIG. 2b, a dipole M^P replaces the X: to form the M^P:R^+-Y^- bond (one can omit the valence sign subsequently for convenience). Atomic or molecular undercoordination results in bond contraction and nonbonding electron polarization[32], making the atom at the topological apex an protruding dipole pointing outwardly[37]. The M^P can point outward or inward of the solid, which determines the subsequent R-Y dipolar orientation. Furthermore, one can replace the M^P with an atomic vacancy V^0 as the vacant edge atoms show stronger resultant effect of polarization with apparent protrusions and the Dirac-Fermon resonant of energy states associated with the core band entrapment and nonbonding polarization for graphite instance [32, 53].

The third situation is the charge polarity inversion, see FIG. 2c. A typical example is the Cu^{+}–O^{2-}:Cu^{P} bond or M^{+}-O^{2-}:M^{p} for general situation of oxygen chemisorption with O^{2-} being an anion and Cu^{p} a dipole (FIG. A1-A2 and Table A1)[21], which meets the force criterion of O^{2-}:Cu^{P} attraction and Cu^{+}—Cu^{P}(positive end) repulsion. The Cu^{+}–O^{2-} dipole induces the Cu atom into a Cu^{P} dipole through the London dispersion force - the instantaneous dipole-induced dipole interaction [54].

4 The O:H-O bond and H_2O irregularities

The equal number of protons and lone pairs allow each H_2O molecule to form a tetrahedral motif with the other four nearest neighbours through O:H-O bonding (Fig. 1a inset). The O:H–O bond is the unique element that carries energy and determines the crystal structure. Any change of the bond angle and the segmental length and energy will transit structural phase and physical properties.

The computational results in FIG. 3a-e confirmed the expected O:H-O segmental cooperative relaxation: the weaker O:H nonbond becomes shorter and stiffer when under mechanical compression and liquid cooling, while the stronger H-O bond expands towards the O:H-O segmental lengths symmetrisation and mass densification. When the transitional quasisolid (QS) phase between liquid and solid cools down, water under molecular undercoordination or electrification, the O—O spacing increases associated with a decrease in mass density, as the O:H–O bond segmental relaxes disparately and contrastingly to the effect of compression. High-energy electron diffraction[14] revealed that a 3315 cm^{-1} laser radiation could relax the H–O and the O:H by ~0.04 Å cooperatively, oppositely, and simultaneously in amplitude on an 80-fatosecond timescale, evidencing the segmental cooperativity.

FIG. 3f shows the O:H–O phonon frequency cooperative thermal relaxation. Heating stiffens the H-O (~3200 cm^{-1}) and softens the O:H (~ 200) and ∠O:H–O bending (~800) cooperatively, indicating that the O:H expands following the regular rule of thermal expansion while the H-O contracts showing the negative thermal expansivity. Sum frequency generation (SFG) spectroscopy has confirmed the essentiality of inter- and intramolecular coupling interactions[55]. The ∠O:H–O bending mode (~1600 cm^{-1}) remains silent. Inset shows the coordination-resolved H-O peak components of bulk (3200), surface (3450), and free H-O radical (3610 cm^{-1}). This set of observations inspired the initiation of the presented coupling O:H-O bond and the HBCP regulation.

Lagrangian-Laplace resolution to the coupling hydrogen bond oscillation dynamics[56] converted the measured segmental length and vibration frequency into the force constant and cohesive energy of the

segment. One can thus obtain the potential paths for the relaxing O:H−O bond, as exemplified in FIG. 3g. Compression shortens the O:H bond and lowers its energy, while the H−O bond, in contrast. Both segments move along the potential curves in the same direction.

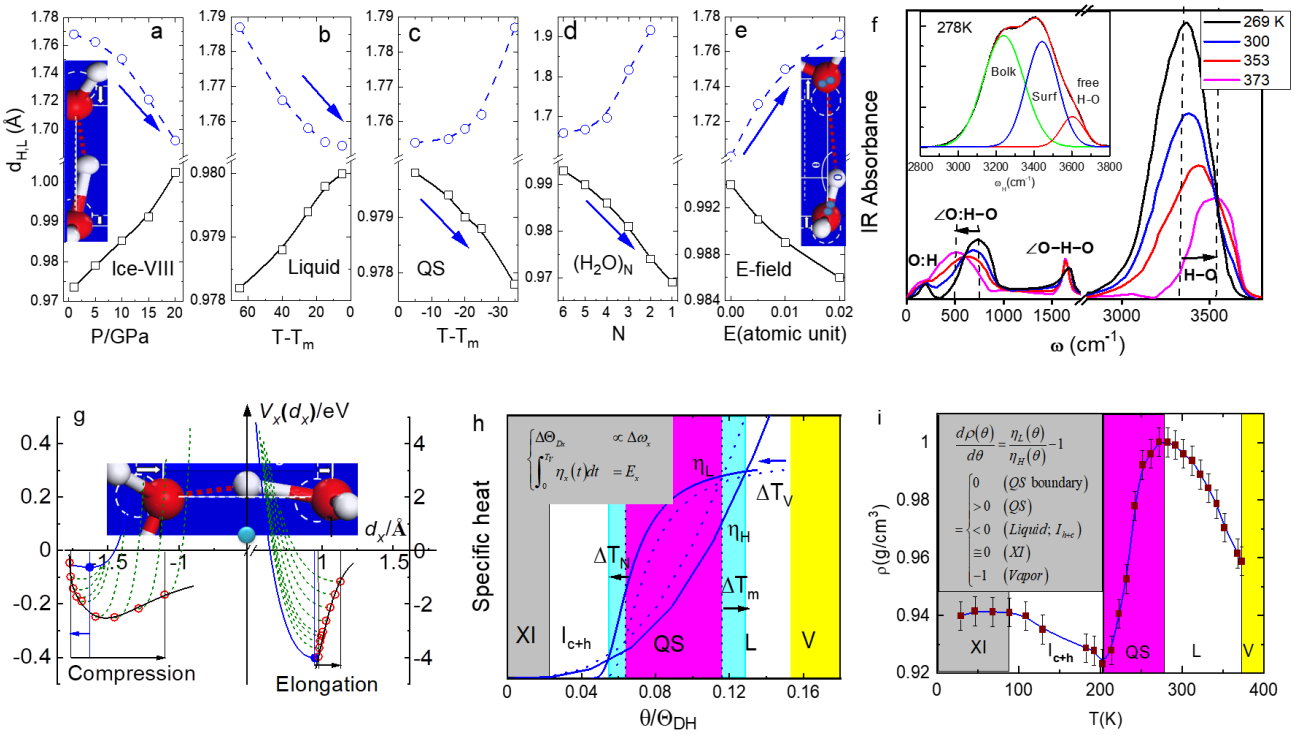

FIG. 3| O:H-O bond cooperative relaxation in the segmental length, energy, vibration frequency, and its functionality on the phase structures and density transition. Segmental length response to (a) Mechanical compression, (b) Liquid and (c) Quasisolid (QS) cooling, (d) molecular undercoordination, and (e) electrostatic polarization. (f) O:H-O vibration frequencies thermal relaxation [23]. (g) Potential paths for the relaxing O:H−O bond under compression (from l. to r.: P = 0–60 GPa[29]) toward segmental lengths symmetrization. Frequency and cohesive energy defined (h) specific heats $\eta_H(\theta, \Theta_{DH})$ and $\eta_L(\theta, \Theta_{DL})$ whose combination specifies the phase boundaries and the exotic QS phase bound at temperatures of extreme densities close to T_m and T_N[31]. (i) Specific heat η_L/η_H ratio determined density thermal evolution of bulk water and 4.4 nm-sized droplet[57] (θ < 277 K), which triggers the QS phase negative thermal expansivity for ice buoyancy. Insets (h and i) show the respective formulations.

The specific heat curves in FIG. 3h interact with each other to form the phase boundaries of Vapor, Liquid, QS, Ice-I, and Ice-XI phases. The exotic QS phase boundaries correspond to temperatures of extreme densities that are close to the temperatures for melting (T_m) and ice nucleation (T_N). The Liquid phase ends at the Vaporization temperature (T_V). The response of the O:H-O segmental

vibration frequency and cohesive energy to perturbation disperses the phase boundaries. The solid lines in the diagram represent the outward dispersion of the QS boundary, which occurs due to factors like electrification, pressure reduction, or molecular undercoordination. These perturbations can lead to surface pre-melting, supercooling at T_N and T_V, and superheating at T_m[12]. Conversely, mechanical compression causes the QS boundaries to move inwardly, leading to ice regelation and instant ice formation[44], as compression lowers the T_m, raises the T_N, and recovers when the pressure is relieved.

The formulation shown in FIG. 3i coordinates the thermal evolution of the mass density of water. The segment with lower specific heat responds regularly to a thermal loading, while the other segment behaves contrastingly due to the O—O repulsive coupling interaction. In the liquid and ice-I phases, where $\eta_L < \eta_H$, the O:H behaves regularly while the H-O exhibits negative thermal expansivity. During the QS phase cooling, the situation reverses since $\eta_L > \eta_H$. Cooling shortens the H-O bond to a lesser degree than the O:H bond expansion. This segmental disparate relaxation results in an expansion of volume and a drop in mass density, which triggers ice buoyancy. In the ice-XI phase, the O:H-O bond remains silent[58] due to the low-temperature approximation of $\eta_L \approx \eta_H \approx 0$.

The HBCP premise ensures the presence of unusual water and ice properties. From FIG. 4a and b, one can see changes in phonon abundance and frequency of H-O bonds from the original state of pure water to the treated specimen. With the perturbative differential phonon spectroscopy (PDPS) [32], one can refine and quantify the phonon abundance transition from the reference to the species after conditioning by integrating the PDPS peak. The PDPS process involved differentiating the reference spectrum from the spectra of treated specimens, with all peak areas normalized.

Electrification or molecular undercoordination shortens the H-O bond and stiffens its phonon, leading to polarization and an 8% elongation of the O—O spacing, according to DFT calculations and XPS measurements??. The relaxation shifts the H-O vibration frequencies from the bulk reference of 3200 to approximately 3450 cm^{-1}. The skins of water and ice[49], the ionic hydration cell[26], and the electrified water bridge[25] share the same H-O bonding identity of undercoordination. An ultra-violet photoelectron spectroscopy examination uncovered that electronic hydration and molecular undercoordination of water droplets lowers the bound energy of a hydrated electron from 2.4 to 1.2 and 0.4 eV when moves from the centre to the skin of a droplet and a $(H_2O)_5$ cluster. [59, 60]

The PDPS analysis[31] of 5% deuterium-contained water droplets ranging from 1.7 to 4.0 nm in size [61] showed that the D-O bond within the skin shell, which is 0.295 nm thick, contracts by 10% from its bulk value of 0.10 nm. This D-O contraction leads to a blue shift in the D-O vibration frequency, from around 2480 to 2600 cm^{-1}, and the H-O phonon lifetime from 2.6 ps for bulk to 50 ps for the 1.7 nm droplet[62].

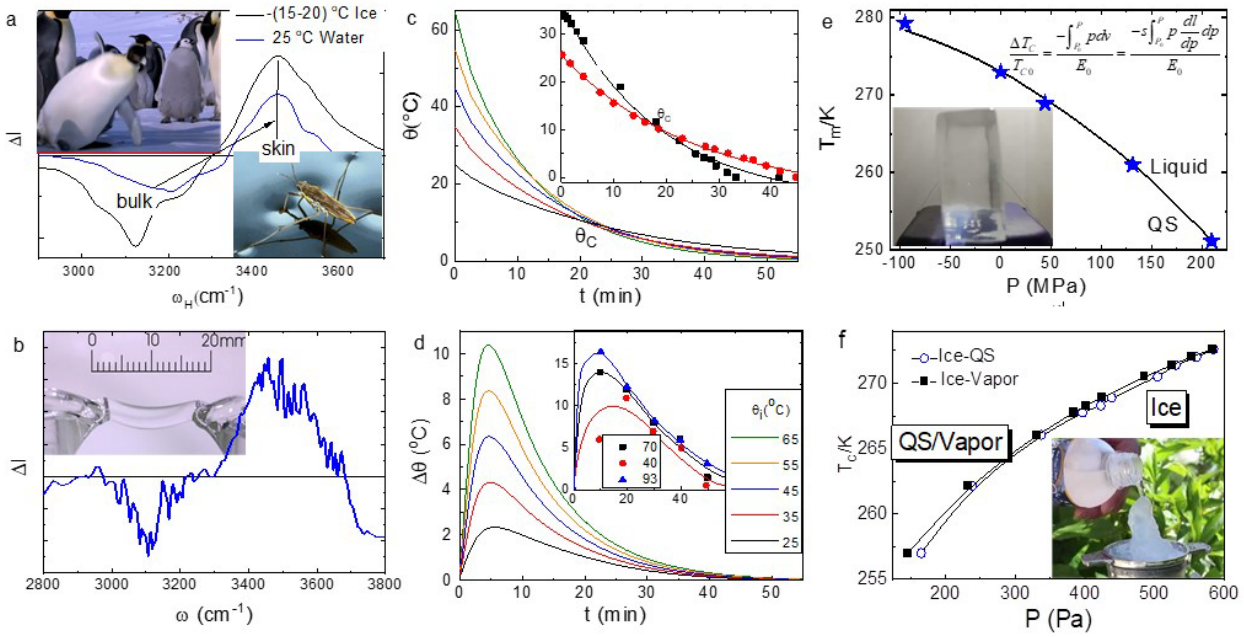

FIG. 4 | Resolution to typical anomalies of water and ice. (a) Water and ice share the same supersolid skin characterized by 3450 cm^{-1} and polarization[63]. The supersolidity of elasticity and electric repulsivity foster the slipperiness of ice[44] and the hydrophobicity and toughness of the water skin. (b) An electrified water bridge[64] showing the same 3450 cm^{-1} feature has a16 MPa elasticity stabilizing at 330 K[65]. The high thermal diffusivity of the skin supersolidity and the O:H-O bond memorability claim the causes of (c, d) Mpemba paradox (insets show observations[66, 67]). Theoretical reproduction[31] of the pressure-induced (e) T_m depression and (f) T_N and T_V elevation resolves the H-O cohesive energy dominance of ice regelation[44] and O:H energy dominance of the instant ice formation [68].

Electrification or molecular undercoordination converts ordinary water into a gel-like, less dense (3/4 unit), hydrophobic, viscoelastic supersolid phase[31]. This supersolid phase is more thermally diffusive and mechanically and thermally stabler than pristine water[69]. The supersolid phase of water ice has a range of remarkable properties. It enhances the dielectric properties of water ice[70], widens the bandgap of ice[71], and increases its catalytic capability and chemical reactivity [72-74]. The supersolid phase also

prolongs the lifetimes of phonons[62] and hydrated electrons[60, 75]. This supersolidity promises 120 K super-elasticity of ice microfibers[42] and 330 K stability of the electrified, highly elastic water bridge over the rims of infilled containers[65].

According to the numerical resolution to Fourier fluid thermodynamics[31], the supersolid skin of 3/4 mass density of the standard raises the thermal diffusivity, $\alpha \propto \rho^{-1}$, that promotes the outward heat flow involved in the Mpemba paradox[66]. The Mpemba paradox shows that warm water cools faster when its initial skin temperature is higher than its interior till an equilibrium. Consistency in theoretical and experimental observations (shown in FIG. 4c and d) [66, 67] clarified that the Mpemba paradox proceeds in the following stages. The H−O bond absorbs energy through thermal contraction, followed by cooling and energy emission in the reverse, at a rate proportional to its initial storage or bond length deformation. The high thermal diffusivity of the liquid skin leads to rapid heat diffusion crossing the supersolid interface. Therefore, the resolution to the Mpemba paradox evidences the O:H−O bond memorability and water skin supersolidity.

To theoretically reproduce the T_C−P ($T_C = T_m$, T_N, and T_V) lines shown in FIG. 4e and f requires the respective $dl/dp > 0$ for T_m depression and $dl/dp < 0$ for T_N and T_V elevation (formulation in the inset of FIG. 4e). Seen the pressure effect on O:H-O relaxation from FIG. 3b, the H−O takes responsibility for the T_m depression, and the O:H for the T_V and T_V elevation. Theoretical matching to the T_C−P curves confirmed that $\Delta T_m \propto \Delta E_H$ and $\Delta T_N \propto \Delta T_V \propto \Delta E_L$, which clarified the bonding origins of ice regelation and instant ice formation (insets FIG. 4e and f) [44]. The compression-derived polarization and O—O contraction opposing the thermal depolarization and O—O expansion cause the least compressibility of water at ~320 K[76].

??

5 Electron lone pair engaged N/O:-H-N/C bond

The PDPS refinement of the $\Delta\omega_H$ in FIG. 5a uncovered that the covalent H-O bond of the O:H-O undergoes thermal contraction and pressure elongation, according to the frequency ω dependence on the length r and energy E of an oscillating on the base of $\omega^2 \propto E/d^2$,[34]

$$\frac{dLn(\omega)}{dLn(r)} = -\left(1 + \frac{r_0}{2E_0}\left|\frac{dE}{dr}\right|\right) = -\left(1 + \frac{1}{2}\left|\frac{dLn(E)}{dLn(r)}\right|\right)$$

The -dE/dr is the force $F(r_0+\delta(q))$ of the relaxed dimer relaxing by a $\delta(q)$ amount under a perturbation q.

The O:H-N bond for the explosive TATB ($C_6H_6N_6O_6$)[35] and LLM-105 ($C_4H_6N_4O_5$)[34] assemblies share similar spectral peak shifts of the O:H−O bond whose covalent part shows negative compressibility and negative thermal expansivity (FIG. 3b). In contrast, the dangling H−N bond in LLM-105 responds to perturbation regularly because of the absence of O:⇔:N coupling, and the dangling H−N bond vibrates at higher frequencies than the covenant part of the O:H-N due to the effect of undercoordination that shortens and stiffens the dangling one. Serving as food additives and fertilizers, Biurea ($C_2H_6N_4O_2$) and Oxamide ($C_2H_4N_2O_2$) also exhibit the ω(P) spectral features of water[77, 78]. In nitromethane (CH_3NO_2)[36], the H−C bond experiences thermal and compression contractions. The compression affects the H−C bond much more than thermal perturbation, as shown in FIG. 5c. This occurrence suggests that the O:⇔C repulsion is insufficiently strong to ensure the HBCP full functioning. The negativity difference between C and H (2.5-2.2 = 0.3) may be too small to ensure the required strong O:⇔C repulsion.

The explosive compound known as full-nitrogen *cyclo*-N_5^- can only be stabilized under acidic conditions by forming c*yclo*-N_5^-:($4H_3O^+$; $3H_3O^+ + 2NH_4^+$) complexes[33, 79, 80]. The force diagram in FIG. 5d shows that the N atom undergoes sp^2-orbital hybridization with its lone pairs occupying the third orbitals in the plane. The circumferential repulsion between protons of the H_3O^+ shortens the H−O bond of the H_3O^+. The combination of the N:⇔:N repulsion, covalent N−N interaction, the aromatic π bonding in the ring, and the radial stretching N:H-O bonds stabilizes the central N_5^- ring.

The resultant force of H↔H repulsions stretches the radial N:H−O bond, which shortens its H−O bond and shifts the lone pairs outwardly (see FIG. 3b reversing pressure direction). The outward shift of the lone pairs weakens the N:⇔:N repulsion and breaks the interaction equilibrium of the N−N that will contract. The interplay between the N:H−O tension and the inter-proton repulsion not only stabilizes the *cyclo*−N_5^- complexes but also stores excessive energy by shortening all covalent bonds. Any N:⇔:N or H↔H disruption can destabilize the system, leading to detonation. The X:H−Y bond structure shall promise structural stability, energy storage, ignition, detonation dynamics, sensitivity to perturbations, and radiation power for the CHNO energetic substance[81, 82].

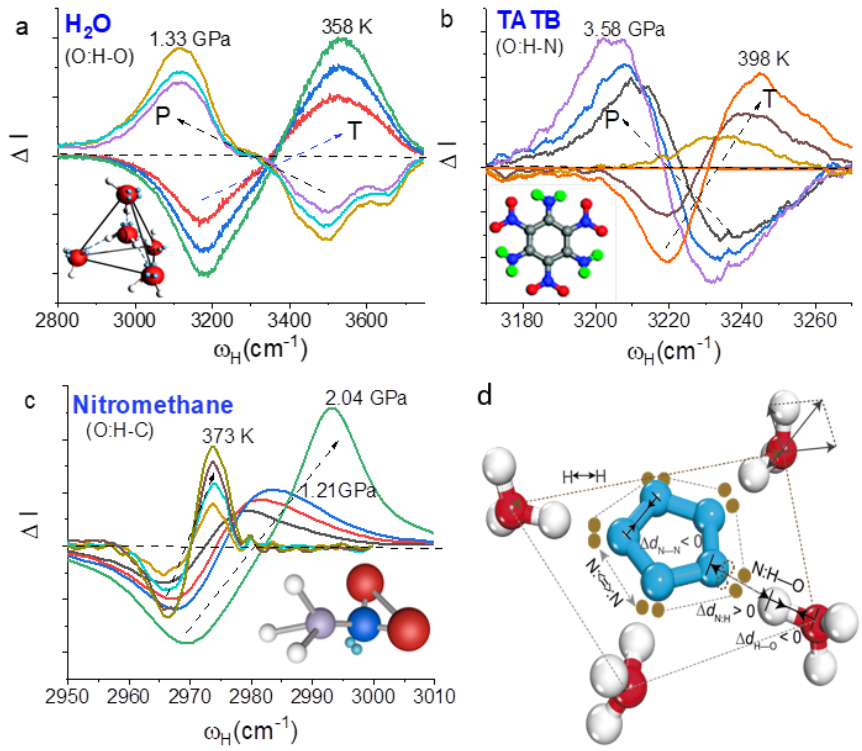

FIG. 5 | Mechanical and thermal response of the H−N/O bond for H_2O and energetic CHNO molecular assemblies. PDPS refinement of the pressure and thermal effects on the ω_H for (a) the H–O bond of H_2O[31], (b) the H−N bond of TATB[35], and (c) the H−C bond of Nitromethane[36]. Compression lengthens and softens the H−N/O bonds while heating does it contrastingly, except for the O:H−C whose H−C contracts under compression and heating because of the insufficient strong O:⇔C repulsion. (d) The resultant force of the circumferential H↔H repulsion stretches the radial N:H–O bond and weakens the N:⇔:N repulsion, which not only stabilizes the *cyclo*−N_5^-:(4~5)H_3O^+ complex [33, 79] but also stores energy by shortening all covalent bonds.

??

6 Hydration interfacial O:H-O bond relaxation

Solvation injects shaped and sized carriers of charge into a solvent to form a sublattice of hydration cells, interlocking with the hydrogen bonding network of the solvent[26]. Hydration of electrons, ions, lone pairs, protons, and molecular dipoles mediates the O:H−O bonding network and properties of the solution through interfacial O:H attraction, H↔H and O:⇔:O repulsion, screened solute polarization by hydrating water dipoles, intra-solute bond contraction, and inter-solute repulsion without any interfacial bond formation. The insets of FIG. 6a-c illustrates the occupancy of charge carriers for the solute of salt, acid, and base, which form the ordered three-dimensional (±; H_3O^+;

HO^-):$4H_2O$:$6H_2O$ hydration cells[26]. The hydrating O:H-O bonds perform differently from the regular ones and determine the functionality of a solution.

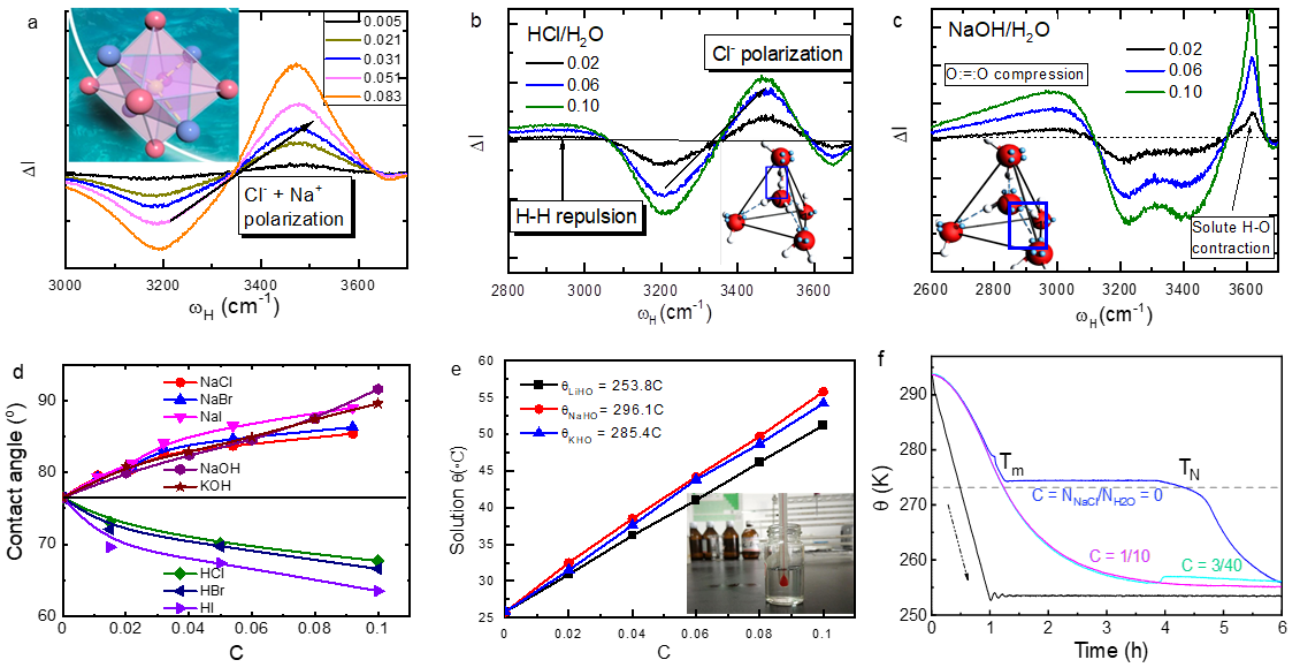

FIG. 6 | Hydration cell bonding characteristics and functionalities. PDPS refinement of the interfacial ω_H for (a) NaCl, (b) HCl, and (c) NaHO solutions with insets showing the respective 3D-(±; H_3O^+; HO^-):$4H_2O$:$6H_2O$ hydration cells. Ionic hydration derives the supersolid hydration cells with (a) characteristic phonon frequencies centered at ~3450 cm^{-1}. Solvation of an acid and base crystal derives the respective H↔H and O:⇔:O repulsions that lengthen the solvent H–O bond (featured at < 3100 cm^{-1}) while the solute H–O bond of the less-ordered HO^- contracts, featured at 3610 cm^{-1}. (d) Ionic or lone pair polarization raises the solution surface stress and viscosity while the H↔H repulsion disrupts the bonding network and surface stress. (e) O:⇔:O repulsion lengthens the solvent H−O bond during base solvation, which releases energy heating the solution. (f) Temperature decay of the quasisolid (plateau) and the supersolid of saturated NaCl solution (molecular ratio concentration C = 1/10) under cooling from 293 down to the maintained 253 K.

Ions occupy eccentrically the interstitial hollow sites to form supersolid hydration cells in which the hydrating O:H−O bond performed the same as its electrification featured at ~3450 cm^{-1}, see FIG. 4b and FIG. 6a. Solvation of an acid or a base crystal introduces excessive protons and lone pairs that form the repulsive H↔H and O:⇔:O, respectively. The H↔H and O:⇔:O repulsions lengthen the annexing H−O bond, as mechanical compression does (FIG. 3b and FIG. 5a), giving rise to the < 3100 cm^{-1} spectral humps whose abundances depend on the strength of the repulsion, see FIG. 6b and c.

The H−O bond of the HO^- solute contracts by 10% due to its bond order loss and the BOLS-NEP regulation, showing the same feature at 3610 cm^{-1} of the dangling H−O bond of water.

The H↔H repulsion that is incapable of polarizing surroundings disrupts the bonding network and surface stress while the ionic and lone pair polarization does it positively (FIG. 6d) and raises solution viscosity that follows the Jones-Dole expression[83], $\eta(C) = aC_+ + bC_-^{1/2}$. The a and b are adjustable parameters. The fully-screened polarization of small cations claims for the linear term C_+, whereas the partially-screened anionic polarization enables the inter-anion repulsion, which claims for the $C_-^{1/2}$ term of the viscosity of alkali-halide salt solutions. The solvent H−O bond emits energy during base solvation by O:⇔:O compressive elongation, instantly heating the solutions (FIG. 6e)[26].

FIG. 6f shows the temperature decay of the pristine water and the saturated NaCl solutions cooled from 293 K down to the maintained 253 K. The H−O bond absorbs energy in the QS phase by spontaneous contraction, leading to a plateau of the cooling profile during aging from $t(T_m)$ and $t(T_N)$. In contrast, the supersolid phase of hydration cells decays exponentially with time, showing that the H−O bond emits energy as it does in the liquid and ice phases by spontaneous cooling expansion (FIG. 3b) without signatures of phase transition.

7 Atomic dipolar substituted M^P:R-Y

According to the BOLS-NEP notion, atomic undercoordination shortens the $Z-X^P$ distance and induces the X^P dipole pointing to R. The combination of X^P:R attraction and X^P⇔Y repulsion stretches and weakens the R−Y dipole. The degree of atomic undercoordination determines the extent of $Z-X^P$ contraction, X^P polarization, the stretching force on R−Y, and hence the efficiency of undercoordinated dipolar catalysis[72, 84].

FIG. 7a and b show the PDPS confirmation of the BOLS-NEP driven Rh 3*d* band splitting into the polarization and entrapment-polarization from the bulk centre of 306.5 eV component and the DFT derived 4*d*5*s* band polarization named *d*-band shifting[85]. The 4*d*5*s* polarization makes the undercoordinated Rh atom a protruding Rh^P dipole that attracts the H and repels the C to form the dipolar-substituted Rh^P:H−C bond during methane physisorption. The Rh^P:H−C system follows the HBCP and BOLS-NEP regulations.

FIG. 7c confirms the RhP:H−C cooperative relaxation as a function of Rh atomic undercoordination, derived from DFT computations. The lower the atomic coordination, the stronger the polarization, and the longer the H-C separation, which is beneficial to H-C bond dissociation.

Therefore, the HBCP and the BOLS-NEP regulate molecular physisorption, which is basis of catalytic capability and chemical reactivity of atoms at the topological apexes. The coupling pair of M^P:R-Y dipoles meet the force criteria and display characteristics for the three-bodied coupling hydrogen bond. The catalysis promotes a reaction without any electron exchange with the reactant elements.

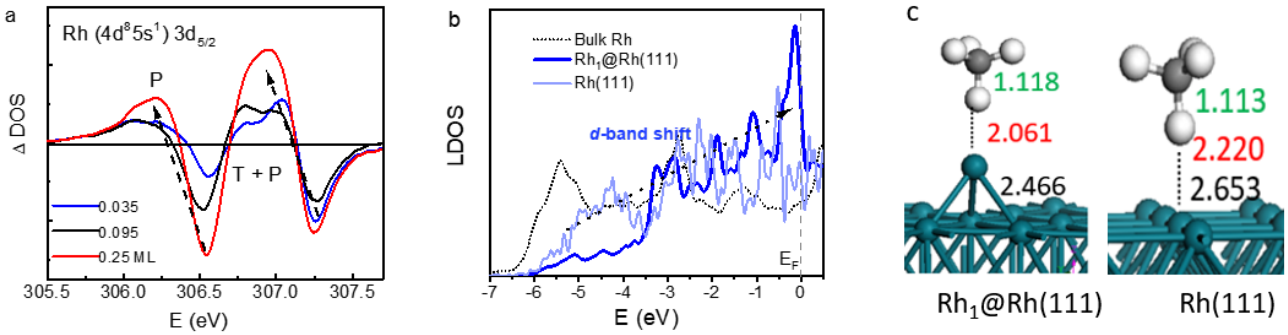

FIG. 7 | BOLS-NEP driven electronic performance of undercoordinated atoms and the dipolar-replaced M^P:R−Y bond. BOLS-NEP regulated (a) Rh adatoms 3*d* band entrapment (T) and polarization (P) measured using XPS[32, 86], (b) the 4*d*5*s* band upward shifting, and (c) Rh_1-Rh bond contraction derived the Rh^P:H-C bond cooperative relaxation.

8 Charge polarity inverted M^+-O^{2-}:M^P bond

The BOLS-NEP and HBCP premises govern not only the process of physisorption but also the bonding and electronic dynamics of oxygen chemisorption.[21] Oxygen chemisorption on the Cu(100;110) surfaces produces the polarity-inverted Cu^+−O^{2-}:Cu^p bonds (see FIG. S1-S2 for detailed information). During the reaction, the Cu^+−O^{2-} bond contracts, and the O^{2-}:Cu^p expands cooperatively, meeting the HBCP regulation. FIG. 8a shows the four-stage Cu_3O_2 and the Cu^+−O^{2-}:Cu^p forming dynamics on the Cu(100) surface resolved using scanning tunneling microscopy (STM) and very low-energy electron diffraction (VLEED) [21]. The dissolved O_2 bonds to the same Cu atom first to form the CuO_2 with an O^-−Cu^{2+} distance of 0.163 nm, or 88% of its bulk reference of 0.185 nm. Then, each O^- bonds to a Cu atom underneath to form the Cu^+−O^{2-} bond that contracts by up to 4%. The sp^3-orbit hybridization only happens once electrons fully occupy the two bonding orbits of the O, which leads to a Cu_3O_2 twin

tetrahedron. Likewise, each O bonds to Cu atoms in the second atomic layer to form the Cu^{+}–O^{2-}:Cu^{P} bond between the outermost two sublayers. The chemisorption vaporizes the alternative row of Cu atoms from the (110) and the every-fourth row of atoms from the Cu(100) surface by atomic isolation and dipolar repulsion[21].

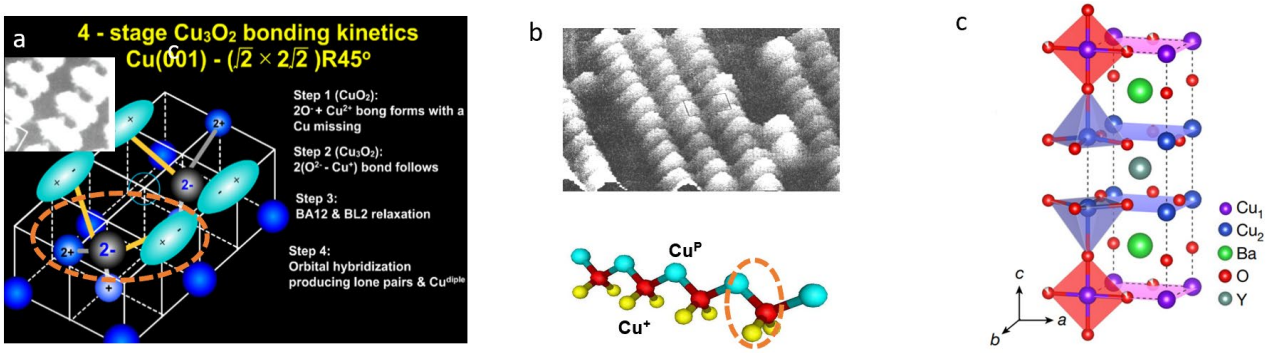

FIG. 8 | BOLS-NEP driven the dipolar-replaced Cu^{+}-O^{2-}:Cu^{P} bond during O-Cu(110; 110) chemisorption. The polarity-inverted Cu^{+}–O^{2-}:Cu^{P} bonds (framed) bridge the outermost two layers of (a) the Cu(100) and (b) the Cu(110) surfaces. The oppositely coupled, dumbbell like Cu^{P}:⇔:Cu^{P} dipoles cross over the missing-row vacancies (open circle) on the Cu(100) surface (FIG. S1-S2), and the Cu^{P}:O^{2-}:Cu^{P} dipolar chain formed between the every-other-row of Cu vacancies on the Cu(110) surface. Atomic undercoordination shortens the Cu^{+}–O^{2-} and lengthens the O^{2-}:Cu^{P}. (c) Crystal structure and the CuO_2 plane of cuprite oxide HTSC[87]. STM images printed with permission from[21, 88, 89].

The Cu^{+}–O^{2-}:Cu^{P} is the exact situation of the polarity-inverted coupling X:R–Y bond. The polarized Cu^{P} points away from O^{2-} to the open end of the surface. The BOLS-NEP-regulated Cu^{+}–O^{2-} contraction lengthens the O^{2-}:Cu^{P} by up to 10% through Cu^{+}⇔Cu^{P}(positive end) repulsive coupling. Therefore, O–Cu(100; 110) chemisorption produces dipoles, ordered atomic vacancies, and the coupling Cu^{+}–O^{2-}:Cu^{P} bonds that follow the HBCP regulation. The Cu^{P}:O^{2-}:Cu^{P} chains sat alongside vacancies on the (110) surface, and the oppositely coupled Cu^{P}⇔Cu^{P} dipoles bridge over the vacant rows of the (100) surface. The chemisorption enlarges the (100) layer spacing from 0.175 to 0.193 nm by 10% through O:Cu^{P} expansion.

Most high temperature super conductors (HTSC) prefer the layered structure with gaps serving as channels for transporting. Dirac fermions of the undercoordinated edge atoms serve as carriers. The topological edge superconductivity (TESC)[90] of FeTeSe and the interface FeAs/$FeLaO_3$[91] share a similar conductance to the Bi-2212 HTSC[92], albeit with different T_C values and resonant peak

separations crossing the Femi energy[90]. The Bi-2212 conductivity is thickness independent. The monolayer Bi-2212 has an identical T_C = 105° K and a resonant peak at 30 meV[92] to its bulk parent[93]. Comparatively, the T_C and the energy gap of the TESC are one order lower than that of cuprite oxides. At the T_C, spin thermal decoupling may happen, and the energy gap disappears. Therefore, both TESC and HTSC share a common origin of atomic undercoordination-induced polarization, albeit T_C values.

Findings in the O−Cu(100; 110) chemisorption may assist in understanding the low-dimensional HTSC and TESC. The Bi-2212 conduction channel is composed of a half-unit cell that contains two CuO_2 planes of mirror symmetry: Cu^{+}−O^{2-}:Cu^{p}:⇔:Cu^{p}:O^{2-}−Cu^{+}, with an association of shorter Cu^{+}−O^{2-} and longer Cu^{p}:O^{2-} in addition to the ordered vacancies and purposed doping. The expanded O^{2-}:Cu^{p}:⇔:Cu^{p}:O^{2-} spacing with ordered vacancies and dopants may offer the required channel for quantum transport.

The spin-resolved electronic polarization of lower effective mass and higher group velocity may act as carriers. The weak O^{2-}:Cu^{p} of 30-80 meV vibrates at much lower frequencies[21]. For reference, the surface O:H nonbond of 100 meV vibrates at ~80 cm^{-1} compared to its bulk of 200 meV and 200 cm^{-1}. The polarization lowers the effective mass that is proportional to the reciprocal curvature of the dispersion curve $E(k)$, $m^*(k) \propto [\nabla_k^2 E(k)]^{-1}$, and raises the group velocity $v(k)$ in the $v(k) \propto \nabla_k E(k)$ form of the locally polarized electrons with k being the wavevector[20]. When excited, the polarized charge carriers of lower effective mass and higher group velocity travel freely and cohesively in the channels under the assistance of the soft and elastic phonons. Interactions between the slow O^{2-}:Cu^{P} oscillators and the polarized electrons might be responsible for the electron-phonon coupling. The oppositely coupled or the paralleled configurated energetic dipoles might promise for the observed pair density waves[94]. The undercoordination-induced bond contraction could clarify the observed "Fermionic attraction" along the monatomic Cu−O chain[95].

One may consider the selectivity of the light elemental constituents of group V-VII. These atoms undergo sp^3-orbital hybridization with a production of nonbonding lone pairs that induce the larger atoms into antibonding dipoles with states near or across the E_f. These localized electrons may have a high chance of forming Cooper pairs under the assistance of the slow and elastic O^{2-}:Cu^{P} phonon. The discovery of monolayer Bi-2212[92], the topological edge UTe_2[94] and FeTeSe[90], and the interface $FeAs/FeLaO_3$[91] superconductivity may evidence the significance of lone pairs of O, Te, Se, and As, and atomic undercoordination contributing to the TESC and HTSC.

The strength of the spin-spin coupling may be related to the coherent peak separation and the T_C. Therefore, the spin coupling in the TESC is weaker than the HTSC because the former has much lower T_C, cohesive energy, and conductivity along the even under-coordinated atoms at edges. Nevertheless, the contribution from the spin-resolved polarization should play dominant roles in the TESC and low-dimensional HTSC. Further verification of expectations would be fascinating and rewarding.

9 Conclusion

In summary, by involving the X:⇔:Y repulsion, one can extend the two-body oriented hydrogen bond X···R to the three-body coupling X:R-Y bond that unites a pair of elastic and polarizable dipoles and being inclusive of the inter- and intra-dipole interaction and their correlation. One can amplify the X:R-Y bond to at least three situations of electron lone pair engagement, dipolar or atomic vacancy replacement, and charge polarity inversion. The decisive factor of the amplified hydrogen bond is the combination of the X:R attraction and X:⇔:Y repulsion regardless of the negativity specificity of the constituent elements, which entitles the X:R-Y bond with disparate geometry, energy and specific heat cooperativity, and polarizability, endowing the extraordinary deformation adaptivity, damage recoverability, perturbation sensitivity, catalytic capability, and chemical reactivity of systems involving the coupling X:R-Y interactions. The amplification has led to substantial improvement in understanding water ice anomalies, hydration interfacial identities, CHNO molecular assembles, molecular physisorption, and oxidation, as well as promising ways of thinking about monatomic catalysis and low-dimensional high-T_C superconductivity. The impact of further extension and application of the X:R-Y bond would be enormous on areas far beyond the presently addressed issues such as cell engineering and life science.

Declaration

No conflicting interest is declared.

Acknowledgment

Profitable communications with Professors Guanghui Zhou, Zhigang Wang, Jun Hu, Haiping Fang, and financial support from the National Natural Science Foundation of China (No. 12150100) are gratefully acknowledged.

References

1. Jeffrey, G. A.; Saenger, W., *Hydrogen bonding in biological structures*. Springer Science & Business Media: 2012.
2. Orgel, L., The Hydrogen Bond. *Rev. Mod. Phys.* **1959,** *31* (1), 100-102.
3. Head-Gordon, T.; Johnson, M. E., Tetrahedral structure or chains for liquid water. *Proc. Natl. Acad. Sci. U.S.A.* **2006,** *103* (21), 7973-7.
4. Debenedetti, P. G.; Klein, M. L., Chemical physics of water. *Proceedings of the National Academy of Sciences* **2017,** *114* (51), 13325-13326.
5. Arunan, E.; Desiraju, G. R.; Klein, R. A.; Sadlej, J.; Scheiner, S.; Alkorta, I.; Clary, D. C.; Crabtree, R. H.; Dannenberg, J. J.; Hobza, P.; Kjaergaard, H. G.; Legon, A. C.; Mennucci, B.; Nesbitt, D. J., Defining the hydrogen bond: An account (IUPAC Technical Report). *Pure Appl. Chem.* **2011,** *83* (8), 1619-1636.
6. Van der Lubbe, S. C.; Fonseca Guerra, C., The nature of hydrogen bonds: A delineation of the role of different energy components on hydrogen bond strengths and lengths. *Chemistry–An Asian Journal* **2019,** *14* (16), 2760-2769.
7. Zhang, Z.; Li, D.; Jiang, W.; Wang, Z., The electron density delocalization of hydrogen bond systems. *Advances in Physics: X* **2018,** *3* (1), 1428915.
8. Sobczyk, L.; Grabowski, S. J.; Krygowski, T. M., Interrelation between H-bond and Pi-electron delocalization. *Chem. Rev.* **2005,** *105* (10), 3513-3560.
9. Morrone, J. A.; Car, R., Nuclear quantum effects in water. *Phys. Rev. Lett.* **2008,** *101* (1), 017801.
10. Markland, T. E.; Ceriotti, M., Nuclear quantum effects enter the mainstream. *Nature Reviews Chemistry* **2018,** *2* (3), 0109.
11. Niu, H.; Yang, Y. I.; Parrinello, M., Temperature dependence of homogeneous nucleation in ice. *Phys. Rev. Lett.* **2019,** *122* (24), 245501.
12. Slater, B.; Michaelides, A., Surface premelting of water ice. *Nature Reviews Chemistry* **2019,** *3* (3), 172-188.
13. Goga, N.; Mayrhofer, L.; Tranca, I.; Nedea, S.; Heijmans, K.; Ponnuchamy, V.; Vasilateanu, A., A review of recent developments in molecular dynamics simulations of the photoelectrochemical water splitting process. *Catalysts* **2021,** *11* (7), 807.
14. Yang, J.; Dettori, R.; Nunes, J. P. F.; List, N. H.; Biasin, E.; Centurion, M.; Chen, Z.; Cordones, A. A.; Deponte, D. P.; Heinz, T. F.; Kozina, M. E.; Ledbetter, K.; Lin, M.-F.; Lindenberg, A. M.; Mo, M.; Nilsson, A.; Shen, X.; Wolf, T. J. A.; Donadio, D.; Gaffney, K. J.; Martinez, T. J.; Wang, X., Direct observation of ultrafast hydrogen bond strengthening in liquid water. *Nature* **2021,** *596* (7873), 531-535.
15. Jabłoński, M., Ten years of charge-inverted hydrogen bonds. *Struct. Chem.* **2020,** *31* (1), 61-80.
16. Civiš, S.; Lamanec, M.; Špirko, V. r.; Kubišta, J. i.; Špet'ko, M.; Hobza, P., Hydrogen Bonding with Hydridic Hydrogen–Experimental Low-Temperature IR and Computational Study: Is a Revised Definition of Hydrogen Bonding Appropriate? *J. Am. Chem. Soc.* **2023,** *145* (15), 8550-8559.
17. McBride, C.; Vega, C.; Noya, E. G.; Ramírez, R.; Sesé, L. M., Quantum contributions in the ice phases: The path to a new empirical model for water—TIP4PQ/2005. *J. Chem. Phys.* **2009,** *131* (2), 024506.
18. Yun, Y.; Khaliullin, R. Z.; Jung, Y., Correlated local fluctuations in the hydrogen bond network of liquid water. *J. Am. Chem. Soc.* **2022,** *144* (29), 13127-13136.
19. Chen, M.; Ko, H.-Y.; Remsing, R. C.; Calegari Andrade, M. F.; Santra, B.; Sun, Z.; Selloni, A.; Car, R.; Klein, M. L.; Perdew, J. P., Ab initio theory and modeling of water. *Proceedings of the National Academy of Sciences* **2017,** *114* (41), 10846-10851.

20. Omar, M. A., *Elementary Solid State Physics: Principles and Applications*. Addison-Wesley: New York, 1993.
21. Sun, C. Q., Oxidation electronics: bond-band-barrier correlation and its applications. *Prog. Mater Sci.* **2003,** *48* (6), 521-685.
22. Yoshimura, Y.; Stewart, S. T.; Somayazulu, M.; Mao, H. K.; Hemley, R. J., Convergent Raman Features in High Density Amorphous Ice, Ice VII, and Ice VIII under Pressure. *J. Phys. Chem. B* **2011,** *115* (14), 3756-3760.
23. Chaplin, M. Water structure and science: http://www.lsbu.ac.uk/water/.
24. Sun, C. Q.; Zhang, X.; Fu, X.; Zheng, W.; Kuo, J.-l.; Zhou, Y.; Shen, Z.; Zhou, J., Density and phonon-stiffness anomalies of water and ice in the full temperature range. *J. Phys. Chem. Lett.* **2013,** *4*, 3238-3244.
25. Ponterio, R.; Pochylski, M.; Aliotta, F.; Vasi, C.; Fontanella, M.; Saija, F., Raman scattering measurements on a floating water bridge. *J. Phys. D: Appl. Phys.* **2010,** *43* (17), 175405.
26. Sun, C. Q., Aqueous charge injection: solvation bonding dynamics, molecular nonbond interactions, and extraordinary solute capabilities. *Int. Rev. Phys. Chem.* **2018,** *37* (3-4), 363-558.
27. Smith, J. D.; Saykally, R. J.; Geissler, P. L., The Effects of Dissolved Halide Anions on Hydrogen Bonding in Liquid Water. *Journal of the America Chemical Society* **2007,** *129*, 13847-13856.
28. Sun, C. Q.; Zhang, X.; Zhou, J.; Huang, Y.; Zhou, Y.; Zheng, W., Density, Elasticity, and Stability Anomalies of Water Molecules with Fewer than Four Neighbors. *J. Phys. Chem. Lett.* **2013,** *4*, 2565-2570.
29. Yoshimura, Y.; Stewart, S. T.; Mao, H. K.; Hemley, R. J., In situ Raman spectroscopy of low-temperature/high-pressure transformations of H2O. *J. Chem. Phys.* **2007,** *126* (17), 174505.
30. Sun, C. Q.; Zhang, X.; Zheng, W. T., Hidden force opposing ice compression. *Chem Sci* **2012,** *3*, 1455-1460.
31. Sun, C. Q.; Huang, Y.; Zhang, X.; Ma, Z.; Wang, B., The physics behind water irregularity. *Physics Reports* **2023,** *998*, 1-68.
32. Liu, X. J.; Zhang, X.; Bo, M. L.; Li, L.; Nie, Y. G.; Tian, H.; Sun, Y.; Xu, S.; Wang, Y.; Zheng, W.; Sun, C. Q., Coordination-resolved electron spectrometrics. *Chem. Rev.* **2015,** *115* (14), 6746-6810.
33. Zhang, L.; Yao, C.; Yu, Y.; Jiang, S.-L.; Sun, C. Q.; Chen, J., Stabilization of the Dual-Aromatic Cyclo-$N5^-$ Anion by Acidic Entrapment. *Journal of physical chemistry letters* **2019,** *10*, 2378–2385.
34. Wang, J.; Zeng, Y.; Zheng, Z.; Zhang, L.; Wang, B.; Yang, Y.; Sun, C. Q., Discriminative Mechanical and Thermal Response of the H-N Bonds for the Energetic LLM-105 Molecular Assembly. *J. Phys. Chem. Lett.* **2023,** *14*, 8555−8562.
35. Tong, Z.; Sun, W.; Li, C.; Tang, Z.; Huang, Y.; Yao, C.; Zhang, L.; Sun, C. Q., O: H-N bond cooperativity in the energetic TATB under mechanical and thermal perturbation. *J. Mol. Liq.* **2022,** *358*, 119169.
36. Tang, Z.; Yao, C.; Zeng, Y.; Huang, Y.; Zhang , L.; Yang, Y.; Sun, C. Q., Anomalous H–C Bond Thermal Contraction of the Energetic Nitromethane. *J. Mol. Liq.* **2020,** *314*, 113817.
37. Sun, C. Q., Size dependence of nanostructures: Impact of bond order deficiency. *Prog. Solid State Chem.* **2007,** *35*, 1-159.
38. Yang, X.; Peng, C.; Li, L.; Bo, M.; Sun, Y.; Huang, Y.; Sun, C. Q., Multifield-resolved phonon spectrometrics: structured crystals and liquids. *Prog. Solid State Chem.* **2019,** *55*, 20-66.
39. Huang, W. J.; Sun, R.; Tao, J.; Menard, L. D.; Nuzzo, R. G.; Zuo, J. M., Coordination-dependent surface atomic contraction in nanocrystals revealed by coherent diffraction. *Nature Materials* **2008,** *7* (4), 308-313.

40. Harich, S. A.; Hwang, D. W. H.; Yang, X.; Lin, J. J.; Yang, X.; Dixon, R. N., Photodissociation of H2O at 121.6 nm: A state-to-state dynamical picture. *J. Chem. Phys.* **2000,** *113* (22), 10073-10090.
41. Teixeira, J., High-pressure physics - The double identity of ice X. *Nature* **1998,** *392* (6673), 232-233.
42. Xu, P.; Cui, B.; Bu, Y.; Wang, H.; Guo, X.; Wang, P.; Shen, Y. R.; Tong, L., Elastic ice microfibers. *Science* **2021,** *373* (6551), 187-192.
43. Schulson, E. M., A flexible and springy form of ice. *Science* **2021,** *373* (6551), 158-158.
44. Faraday, M., Note on Regelation. *Proc. R. Soc. London* **1860,** *10*, 440-450.
45. Helmy, R.; Kazakevich, Y.; Ni, C. Y.; Fadeev, A. Y., Wetting in hydrophobic nanochannels: A challenge of classical capillarity. *J. Am. Chem. Soc.* **2005,** *127* (36), 12446-12447.
46. Song, X.; Basheer, C.; Zare, R. N., Water microdroplets-initiated methane oxidation. *J. Am. Chem. Soc.* **2023,** *145* (50), 27198–27204.
47. Song, X.; Basheer, C.; Xia, Y.; Li, J.; Abdulazeez, I.; Al-Saadi, A. A.; Mofidfar, M.; Suliman, M. A.; Zare, R. N., One-step Formation of Urea from Carbon Dioxide and Nitrogen Using Water Microdroplets. *J. Am. Chem. Soc.* **2023,** *145* (47), 25910–25916.
48. Hao, H.; Leven, I.; Head-Gordon, T., Can electric fields drive chemistry for an aqueous microdroplet? *Nature communications* **2022,** *13* (1), 280.
49. Zhang, X.; Huang, Y.; Ma, Z.; Zhou, Y.; Zheng, W.; Zhou, J.; Sun, C. Q., A common supersolid skin covering both water and ice. *PCCP* **2014,** *16* (42), 22987-22994.
50. S. Narayan; J. Muldoon; M. G. Finn; V. V. Fokin; Kolb, H. C.; Sharpless, K. B., "On Water": Unique Reactivity of Organic Compounds in Aqueous Suspension. *Angew. Chem., Int. Ed.* **2005,** *44*, 3275–3279.
51. Margery Cortes-Clerget ; Julie Yu; Joseph R. A. Kincaid; Peter Walde; Fabrice Gallou; Lipshutz, B. H., Water as the reaction medium in organic chemistry: from our worst enemy to our best friend. *Chem. Sci.* **2021,** *12*, 4237-4266.
52. Sun, C. Q., On the low-dimensional high-T_C superconductivity: bond contraction and dual polarization. *Science Bulletin Express* **2022,** *67* (2), 113-117.
53. Ugeda, M. M.; Brihuega, I.; Guinea, F.; Gómez-Rodríguez, J. M., Missing Atom as a Source of Carbon Magnetism. *Phys. Rev. Lett.* **2010,** *104*, 096804.
54. Wagner, J. P.; Schreiner, P. R., London dispersion in molecular chemistry—reconsidering steric effects. *Angew. Chem. Int. Ed.* **2015,** *54* (42), 12274-12296.
55. Grechko, M.; Hasegawa, T.; D'Angelo, F.; Ito, H.; Turchinovich, D.; Nagata, Y.; Bonn, M., Coupling between intra-and intermolecular motions in liquid water revealed by two-dimensional terahertz-infrared-visible spectroscopy. *Nature communications* **2018,** *9* (1), 885.
56. Huang, Y.; Ma, Z.; Zhang, X.; Zhou, G.; Zhou, Y.; Sun, C. Q., Hydrogen Bond Asymmetric Local Potentials in Compressed Ice. *J. Phys. Chem. B* **2013,** *117* (43), 13639-13645.
57. Mallamace, F.; Branca, C.; Broccio, M.; Corsaro, C.; Mou, C. Y.; Chen, S. H., The anomalous behavior of the density of water in the range 30 K < T < 373 K. *Proc. Natl. Acad. Sci. U.S.A.* **2007,** *104* (47), 18387-91.
58. Medcraft, C.; McNaughton, D.; Thompson, C. D.; Appadoo, D.; Bauerecker, S.; Robertson, E. G., Size and Temperature Dependence in the Far-Ir Spectra of Water Ice Particles. *The Astrophysical Journal* **2012,** *758* (1), 17.
59. Wang, B.; Jiang, W.; Gao, Y.; Zhang, Z.; Sun, C.; Liu, F.; Wang, Z., Energetics competition in centrally four-coordinated water clusters and Raman spectroscopic signature for hydrogen bonding. *RSC Advances* **2017,** *7* (19), 11680-11683.
60. Siefermann, K. R.; Liu, Y.; Lugovoy, E.; Link, O.; Faubel, M.; Buck, U.; Winter, B.; Abel, B., Binding energies, lifetimes and implications of bulk and interface solvated electrons in water. *Nature Chemistry* **2010,** *2*, 274-279.

61. Park, S.; Moilanen, D. E.; Fayer, M. D., Water Dynamics: The Effects of Ions and Nanoconfinement. *J. Phys. Chem. B* **2008,** *112* (17), 5279-5290.
62. Park, S.; Fayer, M. D., Hydrogen bond dynamics in aqueous NaBr solutions. *Proc. Natl. Acad. Sci. U.S.A.* **2007,** *104* (43), 16731-8.
63. Kahan, T. F.; Reid, J. P.; Donaldson, D. J., Spectroscopic probes of the quasi-liquid layer on ice. *J. Phys. Chem. A* **2007,** *111* (43), 11006-11012.
64. Ponterio, R. C.; Pochylski, M.; Aliotta, F.; Vasi, C.; Fontanella, M. E.; Saija, F., Raman scattering measurements on a floating water bridge. *Journal of Physics D-Applied Physics* **2010,** *43* (17), 175405.
65. Fuchs, E. C.; Wexler, A. D.; Paulitsch-Fuchs, A. H.; Agostinho, L. L. F.; Yntema, D.; Woisetschlager, J., The Armstrong experiment revisited. *European Physical Journal-Special Topics* **2014,** *223* (5), 959-977.
66. Mpemba, E. B.; Osborne, D. G., Cool? *Phys. Educ.* **1979,** *14*, 410-413.
67. Bregović, N., Mpemba effect from a viewpoint of an experimental physical chemist. *http://www.rsc.org/images/nikola-bregovic-entry_tcm18-225169.pdf* **2012**.
68. Chen, J.; Nagashima, K.; Murata, K.-i.; Sazaki, G., Quasi-liquid layers can exist on polycrystalline ice thin films at a temperature significantly lower than on ice single crystals. *Crystal Growth & Design* **2018,** *19* (1), 116-124.
69. Pennisi, E., Water's Tough Skin. *Science* **2014,** *343* (6176), 1194-1197.
70. Zha, C. S.; Hemley, R. J.; Gramsch, S. A.; Mao, H. K.; Bassett, W. A., Optical study of H2O ice to 120 GPa: Dielectric function, molecular polarizability, and equation of state. *J. Chem. Phys.* **2007,** *126* (7), 074506.
71. Hermann, A.; Schwerdtfeger, P., Blueshifting the Onset of Optical UV Absorption for Water under Pressure. *Phys. Rev. Lett.* **2011,** *106* (18), 187403.
72. Bregante, D. T.; Chan, M. C.; Tan, J. Z.; Ayla, E. Z.; Nicholas, C. P.; Shukla, D.; Flaherty, D. W., The shape of water in zeolites and its impact on epoxidation catalysis. *Nature Catalysis* **2021,** *4* (9), 797-808.
73. Gong, C.; Li, D.; Li, X.; Zhang, D.; Xing, D.; Zhao, L.; Yuan, X.; Zhang, X., Spontaneous Reduction-Induced Degradation of Viologen Compounds in Water Microdroplets and Its Inhibition by Host–Guest Complexation. *J. Am. Chem. Soc.* **2022**.
74. Colussi, A. J., Mechanism of Hydrogen Peroxide Formation on Sprayed Water Microdroplets. *J. Am. Chem. Soc.* **2023**.
75. Verlet, J. R. R.; Bragg, A. E.; Kammrath, A.; Cheshnovsky, O.; Neumark, D. M., Observation of large water-cluster anions with surface-bound excess electrons. *Science* **2005,** *307* (5706), 93-96.
76. Marion, G. M.; Jakubowski, S. D., The compressibility of ice to 2.0 kbar. *Cold Reg. Sci. Technol.* **2004,** *38* (2-3), 211-218.
77. Yan, T.; Wang, K.; Tan, X.; Yang, K.; Liu, B.; Zou, B., Pressure-Induced Phase Transition in N–H···O Hydrogen-Bonded Molecular Crystal Biurea: Combined Raman Scattering and X-ray Diffraction Study. *The Journal of Physical Chemistry C* **2014,** *118* (28), 15162-15168.
78. Yan, T.; Li, S.; Wang, K.; Tan, X.; Jiang, Z.; Yang, K.; Liu, B.; Zou, G.; Zou, B., Pressure-induced phase transition in N-H...O hydrogen-bonded molecular crystal oxamide. *J. Phys. Chem. B* **2012,** *116* (32), 9796-802.
79. Jiang, C.; Zhang , L.; Sun, C.; Zhang, C.; Yang, C.; Chen, J.; Hu, B., Response to Comment on "Synthesis and characterization of the pentazolate anion cyclo-N5 - in (N5)6(H3O)3(NH4)4Cl". *Science* **2018,** *359*, 8953-8955.
80. Zhang, C.; Sun, C.; Hu, B.; Yu, C.; Lu, M., Synthesis and characterization of the pentazolate anion cyclo-N_5^- in (N5) 6 (H3O) 3 (NH4) 4Cl. *Science* **2017,** *355* (6323), 374-376.
81. Liu, G.; Wei, S.-H.; Zhang, C., Review of the Intermolecular Interactions in Energetic Molecular Cocrystals. *Crystal Growth & Design* **2020,** *20* (10), 7065-7079.

82. Xie, Z.-m.; Wang, T.-w.; Du, Y.-b.; Lu, Z.-j.; Wu, X.-w.; Chen, Y.-b.; Zhang, J.-G., Structural, vibrational and electronic properties of nitrogen-rich 2, 4, 6-triazide-1, 3, 5-triazine under high pressure. *J. Mol. Model.* **2023,** *29* (8), 257.
83. Jones, G.; Dole, M., The viscosity of aqueous solutions of strong electrolytes with special reference to barium chloride. *J. Am. Chem. Soc.* **1929,** *51* (10), 2950-2964.
84. Wang, A.; Li, J.; Zhang, T., Heterogeneous single-atom catalysis. *Nature Reviews Chemistry* **2018,** *2* (6), 65-81.
85. Hammer, B.; Norskov, J. K., Why gold is the noblest of all the metals. *Nature* **1995,** *376* (6537), 238-240.
86. Baraldi, A.; Bianchettin, L.; Vesselli, E.; de Gironcoli, S.; Lizzit, S.; Petaccia, L.; Zampieri, G.; Comelli, G.; Rosei, R., Highly under-coordinated atoms at Rh surfaces: interplay of strain and coordination effects on core level shift. *New Journal of Physics* **2007,** *9*, 143.
87. Wang, Z.; Pei, K.; Yang, L.; Yang, C.; Chen, G.; Zhao, X.; Wang, C.; Liu, Z.; Li, Y.; Che, R., Topological spin texture in the pseudogap phase of a high-T c superconductor. *Nature* **2023,** *615* (7952), 405-410.
88. Jensen, F.; Besenbacher, F.; Laegsgaard, E.; Stensgaard, I., Dynamics of oxygen-induced reconstruction of Cu(100) studied by scanning tunneling microscopy. *Phys. Rev. B* **1990,** *42* (14), 9206-9209.
89. Kuk, Y.; Chua, F. M.; Silverman, P. J.; Meyer, J. A., O chemisorption on Cu(110) by scanning tunneling microscopy. *Phys. Rev. B* **1990,** *41* (18), 12393-12402.
90. Lv, B.; Qian, T.; Ding, H., Angle-resolved photoemission spectroscopy and its application to topological materials. *Nature Reviews Physics* **2019,** *1* (10), 609-626.
91. Song, Y.; Chen, Z.; Zhang, Q.; Xu, H.; Lou, X.; Chen, X.; Xu, X.; Zhu, X.; Tao, R.; Yu, T., High temperature superconductivity at FeSe/LaFeO3 interface. *Nature Communications* **2021,** *12* (1), 1-8.
92. Yu, Y.; Ma, L.; Cai, P.; Zhong, R.; Ye, C.; Shen, J.; Gu, G. D.; Chen, X. H.; Zhang, Y., High-temperature superconductivity in monolayer $Bi_2Sr_2CaCu_2O_{8+\delta}$. *Nature* **2019,** *575*, 156-163.
93. Sato, T.; Matsui, H.; Nishina, S.; Takahashi, T.; Fujii, T.; Watanabe, T.; Matsuda, A., Low Energy Excitation and Scaling in $Bi_2Sr_2Ca_{n-1}Cu_nO_{2n+4}$ (n = 1–3): Angle-Resolved Photoemission Spectroscopy. *Phys. Rev. Lett.* **2002,** *89* (6), 067005.
94. Gu, Q.; Carroll, J. P.; Wang, S.; Ran, S.; Broyles, C.; Siddiquee, H.; Butch, N. P.; Saha, S. R.; Paglione, J.; Davis, J. C. S.; Liu, X., Detection of a pair density wave state in UTe2. *Nature* **2023,** *618* (7967), 921-927.
95. Chen, Z.; Wang, Y.; Rebec, S. N.; Jia, T.; Hashimoto, M.; Lu, D.; Moritz, B.; Moore, R. G.; Devereaux, T. P.; Shen, Z.-X., Anomalously strong near-neighbor attraction in doped 1D cuprate chains. *Science* **2021,** *373* (6560), 1235-1239.

Appendices

Polarity-inverted $Cu^{+}–O^{2-}:Cu^{P}$ bond formation during chemisorption [21] and its cooperativity and polarizability

The HBCP[31] and the BOLS-NEP[32] premises govern the processes of O-Cu(001) chemisorption and other surfaces [21]. The reaction creates the coupling $Cu^{+}–O^{2-}:Cu^{P}$ bonds of polarity inversion and dipolar replacement. The bond links the outermost two atomic layers, together with missing row vacancies and outward pointing dipoles. A combination of STM and LEED has quantified four-stage Cu_3O_2 formation on the Cu(001) surface transiting from O^{-} to O^{2-} with the production of the oppositely paired $Cu^{P}⇔Cu^{p}$ dipoles crossing the missing rows.

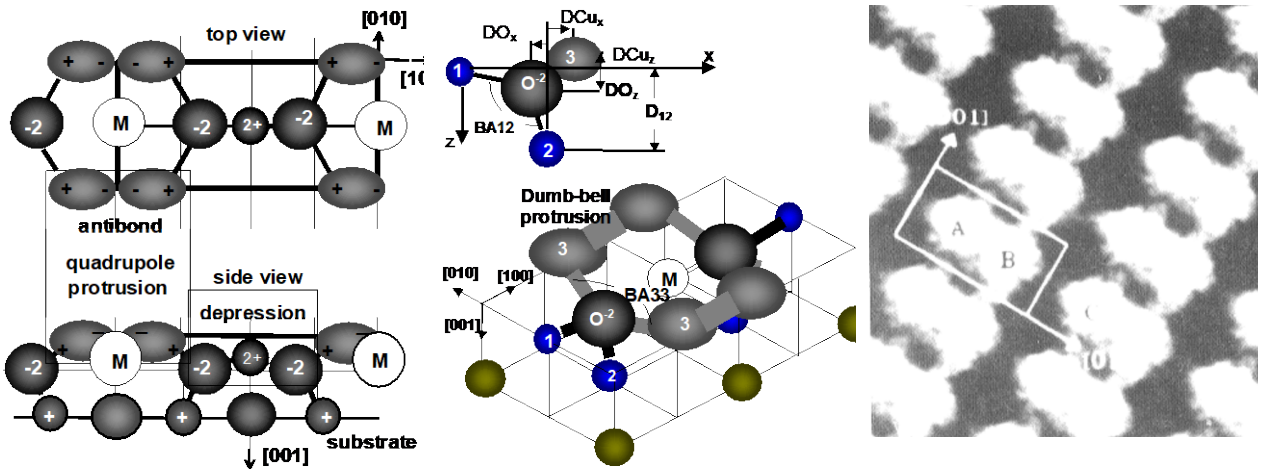

FIG. S1 Top and side views of the structure model and parameters for the Cu_3O_2 on O-Cu(001) surface [21]. Structural configuration for **a**, Cu(001)-(2√2×√2)R45°−$2O^{2-}$ reaction, and **b**, the parameters for LEED calculations. The coupling $Cu^{+}–O^{2-}:Cu^{P}$ bond bridges the outermost two atomic layers of the Cu(001) surfaces, and the oppositely couple $Cu^{P}⇔Cu^{P}$ dipoles cross over the every-fourth missing row of Cu(001), giving rise to the STM image of (c). Undercoordination shortens the $Cu^{+}–O^{2-}$ while the $Cu^{+}⇔Cu^{P}$(positive end) repulsion lengthens the $O^{2-}:Cu^{P}$ cooperatively. The polarity-inverted $Cu^{+}–O^{2-}:Cu^{P}$ bond follows both the HBCP[31] and the BOLS-NEP scaling regulations [32]. The Cu(001)-(2√2×√2)R45°−$2O^{-2}$ reaction proceeded in the ways of [21]:

O_2 (adsorbate) + 4 Cu (surface) + 2 Cu (substrate)
⇒ 2 O^{-2} (hybrid) + Cu^{+2} (surface) + 2 Cu^{+} (substrate)-------(Cu_3O_2 bonding)
+ 2 Cu^{p} (buckled up and crossing the MR) + Cu (vacancy) -(bonding effect).

The O^{-2} prefers the center of a quasi-tetrahedron. Atoms 1 and 2 are Cu^{+2} and Cu^{+}. Atom 3 is Cu^{p} dipole and M is the Cu vacancy arising from the isolation of this atom and repulsion from Cu^{P}. Atom 4 is a metallic Cu atom. The oppositely coupled 3↔3 for $Cu^{P}⇔Cu^{P}$ dipoles bridge over the MR vacancy.

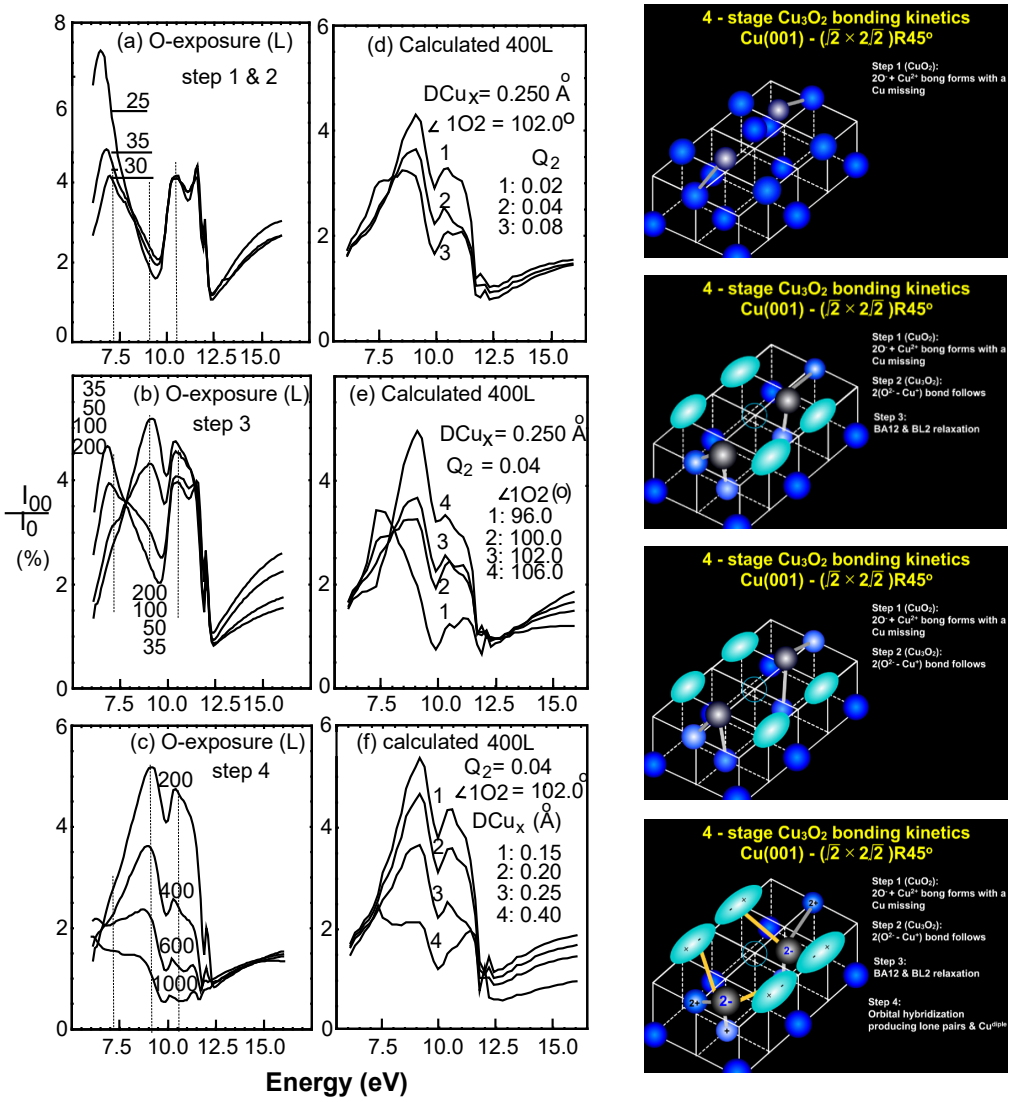

FIG. S2 | Cooperative relaxation of the polarity-inverted Cu^{+}–O^{2-}:Cu^{P} bond [21]. LEED spectral intensities (a-c) at 7.1, 9.1, and 10.3 eV show four discrete reaction stages for the O–Cu (001) surface. d-f Calculated results from varying individual bond variables of bond contraction coefficient Q_2, bond angle ∠1O2 and dipolar dislocation DCu_x for 400 L oxygen-exposure provide the resemblance of the measurements at different stages with output in Table 1.

1) $\Theta_O \leq 30$ L: The 7.1 eV peak intensity decreases and disappears at 30 L, while other peaks remain (a).
2) 30 L > $\Theta_O \leq 35$ L: The 7.1 eV peak intensity recovers slightly, and rest remain (a).
3) 35 L > $\Theta_O \leq 200$ L: The 7.1 eV peak attenuates while one new peak at 9.1 eV emerges; and then both the 9.1 eV and the 10.3 eV peak intensities increase up to their maxima at 200 L.
4) Θ_O > 200L: The entire spectrum attenuates.

TAB S1 | LEED derived four-stage O-Cu(001) surface bonding dynamics. Parameters are specified in FIG. S1b. [21]

Reaction stages	Parameter	1 (< 30 L: BL1 formation); 2 (30 ~ 35 L: BL2 & ∠1O2 change); 3 (35 ~ 200 L: ∠1O2 expansion); 4 (> 200L: DCu_x increase)								
Exposure	(L)	25	30	35	50	100	200	400	600	≥800
Bond contraction	Q_2	0	0	0.04	0.04					
Bond angle (°)	BA12	92.5	94.0	98.0	100.0	101.0	102.0			
Q_1 = 0.12	DCu_x	0.125	0.150	0.150	0.150	0.150	0.150	0.250	0.355	0.450
Atomic dislocation (Å)	$-DCu_z$	0.1460	0.1440	0.1268	0.0938	0.0844	0.0709	0.1495	0.2239	0.2849
	$-DO_x$	0.1814	0.1796	0.1802	0.1831	0.1852	0.1877			
	DO_z	-0.0889	-0.0447	0.0618	0.1158	0.1422	0.1682			
Layer spacing	D_{12}	1.7522	1.7966	1.8287	1.8824	1.9086	1.9343			
Bond length (Å)	BL1	1.628								
	BL2	1.850		1.776						
	BL3	1.8172	1.8326	1.8833	1.8983	1.9053	1.9121	1.9262	1.9396	1.9505
Bond angle (°)	BA13	95.70	98.82	104.24	105.12	105.64	105.33	105.30	104.01	103.83
	BA23	91.80	93.11	95.75	96.46	96.83	95.18	99.52	101.67	103.43
	BA33	165.87	160.83	145.26	144.32	143.02	141.82	139.43	135.38	135.71

*Vacant space is identical in value to that in the previous cell. All information is provided by fine-tuning (BA12, Q_2, DCu_x) variables.